2017 IEEE/RSJ International Conference on Intelligent Robots and Systems (IROS)
September 24–28, 2017, Vancouver, BC, Canada

Energy Characterization of a Transformable Solar-Powered Unmanned Aerial Vehicle

Devon Jenson, Ruben D'Sa, Travis Henderson, Jack Kilian, Bobby Schulz, and Nikolaos Papanikolopoulos
{ jens1172 | dsaxx005 | hende471 | kilia025 | schu3119 }@umn.edu, {npapas}@cs.umn.edu
Department of Computer Science and Engineering, University of Minnesota

***Abstract*— Given the wide variety of flight conditions typically encountered by fixed-wing aerial vehicles, the flight performance of a solar-powered unmanned aerial vehicle (SUAV) depends on many factors. Predicting the performance for a given application requires characterization of both system and environmental components. Furthermore, a SUAV with a transformable airframe increases the number of characterizable states, where each state features a unique set of capabilities. This results in significant differences with respect to power consumption, solar panel orientation, and increases the design limitations on system components.**

This paper characterizes the energy collection, propulsion, and power electronics subsystems of a transformable SUAV developed at the University of Minnesota. Clear-sky and solar panel models are used to predict the power available for a given location and time. Propulsion system design is validated with flight data, and a proposed model correlates propulsion limits with available energy. Power electronics are modeled and simulated to determine hardware and tracking algorithm efficiencies. Finally, a pulsed battery charging methodology is implemented in hardware and evaluated against conventional charging techniques.

I. INTRODUCTION

Over the last several years, unmanned aerial vehicles (UAVs) of various types have been developed for a number of applications. These systems have largely fallen into two main categories: high endurance or high versatility. Recent designs in the high-endurance category have demonstrated the dramatic benefit of solar energy harvesting as a means of extending flight time [1]. However, these types of UAVs are not well suited to applications where stationary positioning is required. The second category of UAVs has seen remarkable progress in the last two decades due to the availability of high-power-density electric propulsion systems [2] and the development of control methods for autonomously navigating flight states in vertical take-off and landing (VTOL) maneuvers [3]. While some current aircraft and rotorcraft designs are capable of many mission maneuvers that conventional high-endurance UAVs cannot perform, the cost of this flexibility comes at the stiff expense of flight time.

The Solar UAV Quad (SUAV-Q) is a design that combines the strengths of both UAV categories. It was first proposed in [4] and is capable of transforming between quad-rotor and fixed-wing configurations (see Figure 1a). This energy hierarchy allows the system to cover large distances in a fixed-wing state and perform stationary operations in a quad-rotor state. Improvements were made to the design in [5] and [6], notably the addition of variable-pitch propellers and modular payload bay design.

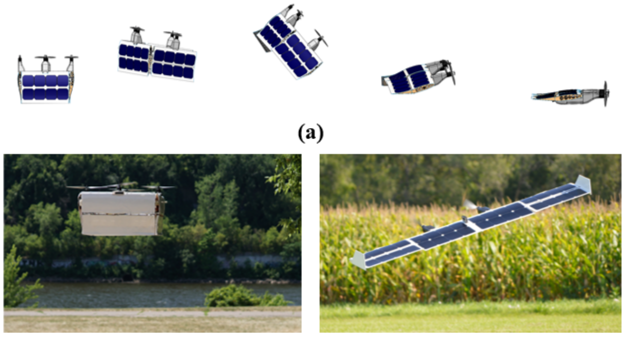
(a)
(b)
(c)

Fig. 1: **(a)** Illustration of SUAV-Q airframe transforming from quad-rotor to fixed-wing flight states. **(b)** and **(c)** SUAV-Q prototypes flying in quad-rotor and fixed-wing configuration at low-altitude.

This paper presents an energy analysis of the SUAV-Q and its core subsystems. The analysis considers the effects of payload mass, battery capacity, and time of year. In addition, experimental evidence using variable-pitch propellers and pulse battery charging is showcased. Concurrent with this work, multiple prototypes were constructed (see Figures 1b and 1c) to validate system operation in quad-rotor and fixed-wing states.

The paper is organized as follows. Section II introduces the SUAV-Q and its design constraints. Clear-sky solar radiation and single-diode solar panel models are used in Section III to predict the energy harvested in both quad-rotor and fixed-wing states. Section IV correlates the effects of battery charge state with the ability of the propulsion system to achieve high-energy operating conditions. Section V considers the efficiency of custom maximum power point trackers (MPPTs) and looks at their tracking efficiency for a number of algorithms. Finally, in Section VI, the benefit of pulse charging on battery lifetime is discussed using a custom hardware design.

II. TRANSFORMABLE SMALL-SCALE UAV TOPOLOGY

The SUAV-Q is capable of operating in any of its four states: fixed-wing aerial, quad-rotor aerial, fixed-wing ground, or quad-rotor ground as shown in Figure 2. The advantage of this airframe is that it can utilize any of these states to meet mission objectives or to maintain desired energy levels. If the batteries are highly discharged in quad-rotor state, the SUAV-Q can land, absorb solar radiation in either quad-rotor or prone configurations, and then take off vertically when enough energy has been gathered. If the

978-1-5386-2682-5/17/$31.00 ©2017 IEEE

mission requires high-endurance as well as precise maneuvers, the SUAV-Q can fly in a fixed-wing state to conserve power and transform, as needed, into a quad-rotor state for high maneuverability. This superior functionality introduces design constraints not traditionally present on solar UAVs. System specifications of the SUAV-Q prototype are listed in Table I.

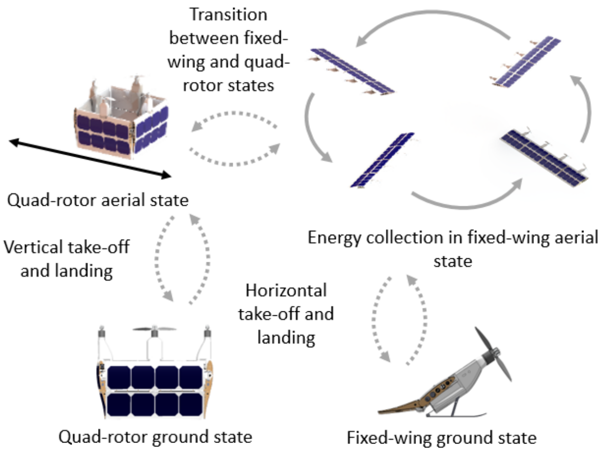

Fig. 2: CAD design of the four steady-state operating modes of the SUAV-Q. Transition from fixed-wing aerial to a ground state can be performed by either transforming into quad-rotor state and vertically landing or performing a traditional horizontal landing. Take-off from a fixed-wing ground state is made possible by a 4-bar servo actuated skid mounted in one of the four pods.

In order to ensure that solar cells are grouped according to irradiance similarity, each wing segment on the SUAV-Q contains eight series-connected SunPower E60 solar cells. Additionally, each wing segment contains its own MPPT as the solar panels can be oriented in completely different directions in quad-rotor state (as shown in Figure 2). Because fixed-wing and quad-rotor flight exhibit dissimilar power consumption characteristics [5], variable-pitch propellers are used to achieve efficient propulsion across flight states. In spite of the frequent charge cycling that is likely on the SUAV-Q platform, battery cycle life is maintained through pulse charging techniques. As illustrated in Figure 3, these four aspects contribute to the SUAV-Q's energy performance. An efficient algorithmic and hardware design approach will be discussed for each of these core system components in the following sections.

System Specifications	Fixed-wing	Quad-rotor	Value
Length	0.51	0.51	m
Wingspan	2.15	0.51	m
Chord Length	0.31	0.31	m
Height	0.09	0.53	m
Battery Mass	232.5	232.5	g
Total Mass	2420	4274	g
Cruise Speed	11.95	N/A	m/s
Stall Speed	9.71	N/A	m/s

TABLE I: System specifications of the SUAV-Q airframe prototype used in this paper's work.

III. SOLAR RADIATION MODEL

A solar radiation model can be used to predict the solar energy incident on a surface. The radiation depends on the time of day, atmospheric conditions, location, and surface orientation. Radiation incident on a surface is commonly modeled as being composed of direct, diffuse, and reflected components. A clear-sky radiation model estimates these components for a given day and geographic location. In this section a radiation model is applied to the SUAV-Q in order to estimate the energy available in quad-rotor and fixed-wing states. Additionally, a single-diode solar panel model is used to determine the electrical power received after conversion and to predict the maximum power operating point for each solar panel.

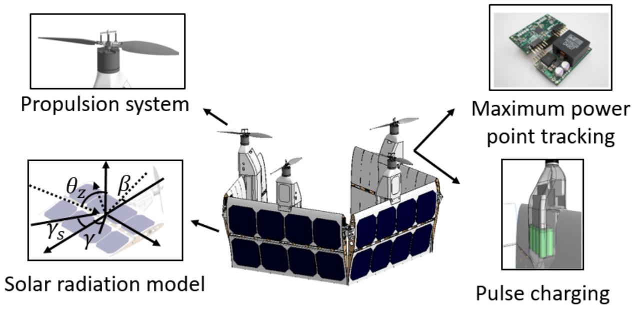

Fig. 3: Primary components of energy management on the SUAV-Q pursued from a hardware and algorithmic perspective.

A. *Irradiance on a Tilted Surface*

Direct (or beam) radiation is the received radiation that has not been scattered by the atmosphere. The relationship between direct radiation and panel orientation is usually described in terms of azimuth and zenith angles. These angles are labeled in Figure 3.

Solar zenith and azimuth angles can be calculated for any time and geographical location by using an ephemeris function (in this model, the PyEphem Python package was used). From these angles, the angle of incidence θ of direct beam radiation on a surface is given in [7] by,

$$\cos\theta = \cos\theta_z\cos\beta + \sin\theta_z\sin\beta\cos(\gamma_s-\gamma)\ . \tag{1}$$

Using the angle of incidence θ, the beam irradiance incident on a tilted surface is given by,

$$G_b = G_{bn}\cos\theta \tag{2}$$

where G_{bn} is the beam irradiance (W/m^2) from the direction of the sun, as determined by the clear-sky model in the next subsection.

Diffuse radiation is the received radiation that has been scattered by the atmosphere. Using the Reindl model [7], the diffuse irradiance is given by,

$$G_d = G_{dh}\left\{(1-A_i)\left(\frac{1+\cos\beta}{2}\right)\left[1+f\sin^3\frac{\beta}{2}\right]+A_iR_b\right\} \tag{3}$$

where A_i is the anisotropy index defined as the ratio of the beam irradiance to the extraterrestrial irradiance G_{bn}/G_o, f is a factor that accounts for cloudiness defined as the ratio of the beam irradiance to the total irradiance on a horizontal surface $\sqrt{G_b/G}$, R_b is the ratio of total irradiance on a tilted surface to the total irradiance on a horizontal surface $\cos(\theta/\theta_z)$, and G_{dh} is the diffuse irradiance on a horizontal surface (W/m^2) determined by the clear-sky model.

B. Clear-Sky Model

To calculate the irradiance components reaching the ground, atmospheric attenuation of the extraterrestrial radiation must be considered. Models vary in the required information and computation time. The Simplified Solis model [8] was chosen due to the availability of column water vapor and aerosol optical depth (AOD) data found in the Typical Meteorological Year 3 dataset (TMY3) [9] and its ease of implementation using the PVLIB Python package [10]. Through evaluation it has been found that including AOD and water vapor significantly improves the accuracy of the clear-sky model [11]. The model calculates an enhanced extraterrestrial irradiance G'_o (W/m^2) as follows,

$$G'_o = G_o\left[a_{700}^2 G_{o2} + a_{700} G_{o1} + G_{o0} + 0.071\ln(p/po)\right] \tag{4}$$

$$G_{o0} = 1.08w^{0.0051},\ G_{o1} = 0.97w^{0.032},\ G_{o2} = 0.12w^{0.56} \tag{5}$$

where G_o[1] is the extraterrestrial irradiance (W/m^2), a_{700} is the aerosol optical depth at 700 nm (dimensionless), p is the atmospheric pressure at the considered altitude (Pa), p_0 is the atmospheric pressure at sea level (Pa), and w is the total column water vapor (cm).

The normal beam, horizontal diffuse, and global horizontal irradiance components are given by the following equations,

$$G_{bn} = G'_o e^{-\frac{\tau_b}{\sin^b h}} \qquad G_{dh} = G'_o e^{-\frac{\tau_d}{\sin^d h}} \tag{6}$$

$$G_{gh} = G'_o e^{-\frac{\tau_g}{\sin^g h}} \sin h \tag{7}$$

where h is the apparent elevation angle of the sun (90°-θ_z) and τ_b, τ_d, and τ_g are the beam, diffuse, and global total optical depths, and b, d and g are fitting parameters obtained from Radiative Transfer Model (RTM) calculations[2].

C. Single-Diode Solar Panel Model

A solar panel, with output voltage V_{PV} and current I_{PV}, can be modeled as the single-diode equivalent circuit [12] shown in Figure 4 and defined by,

$$I_{PV} = I_L - I_o\left(e^{\frac{V_{PV}+I_{PV}R_s}{a}} - 1\right) - \frac{V_{PV}+I_{PV}R_s}{R_{sh}} \tag{8}$$

where I_L is the light current (A), R_{sh} is the shunt resistance (Ω), R_s is the series resistance (Ω), I_o is the reverse saturation current of the diode, and a is termed the diode ideality factor (eV) defined as,

$$a = \frac{N_s n_I k T_c}{q} \tag{9}$$

where N_s is the number of solar cells in series, n_I is the usual diode ideality factor, k is the Boltzmann constant, T_c is cell temperature, and q is electron charge.

The reference parameters[3] for SunPower E60 cells were found by solving the nonlinear equations in [12] with the E60 datasheet parameters. The datasheet parameters for a single cell, listed in Table II, are defined as the open-circuit voltage V_{oc}, short-circuit current I_{sc}, maximum power voltage V_{mp} and current I_{mp}, short-circuit current temperature coefficient α_{isc}, and open-circuit voltage temperature coefficient β_{voc}. The calculated reference parameters are listed in Table III. To compute the I-V curve for an arbitrary incident irradiance and cell temperature, the reference parameters are scaled according to the equations in [12] and Equation 8 is solved by means of the Lambert W function [13] [14] [15]. Figure 5 compares I-V curves computed with the model against actual E60 curves measured at various irradiances and temperatures with a variable load. The series resistance of the model was increased to 0.327 Ω to account for the wire between the load and solar cells.

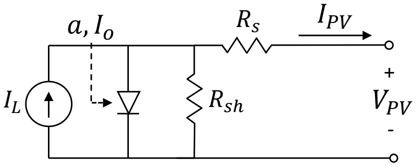

Fig. 4: Single-diode solar cell model

V_{oc}	0.73 [V]
I_{sc}	6.17 [A]
V_{mp}	0.63 [V]
I_{mp}	5.86 [A]
α_{isc}	+0.00054 [A/K]
β_{voc}	-0.0648 [V/K]

TABLE II: E60 datasheet parameters

a_{ref}	0.027141253 [eV]
$I_{L,ref}$	6.17 [A]
$I_{o,ref}$	$1.262\cdot10^{-11}$ [A]
$R_{sh,ref}$	11.8 [Ω]
$R_{s,ref}$	0.08382 [Ω]

TABLE III: Reference parameters

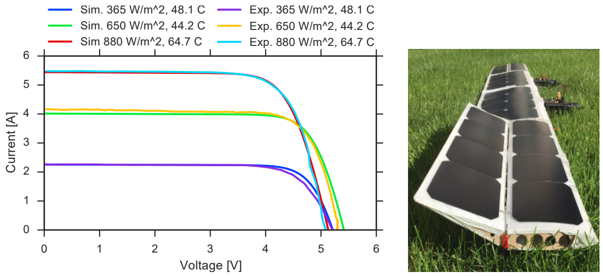

(a) Comparison of solar panel model and experimental E60 I-V curves.

(b) Mounted E60 solar cells

Fig. 5: Comparison of E60 solar cell model (R_s increased to 0.327 Ω) with experimental data.

D. Solar Energy in Quad-Rotor and Fixed-Wing States

Using the described radiation and single-diode models, the received power was simulated for quad-rotor and fixed-wing states located in St. Paul, Minnesota (latitude: 44.933, longitude: -93.05, and altitude: 220 m). For fixed-wing the the panels were assumed to be oriented horizontal to the surface of the earth with a surface tilt of $\beta = 0°$. In quad-rotor state all four panels were assumed to stand at a surface tilt of 90° and face opposite directions (azimuth angles γ = 0°, 90°, 180°, and 270°). Aerosol and water precipitation data was taken from the TMY3 dataset (St. Paul Downtown Airport) [9].

To summarize the model implementation:

1) Compute the solar zenith angle, azimuth angle, and extraterrestrial irradiance using PyEphem

---

[1] 1367 W/m^2 nominal, changes with the earth-sun distance.

[2] The optical depths and fitting parameters are functions of aerosol optical depth at 700 nm, column water vapor (cm), and pressure (Pa), see [8] for additional details.

[3] Reference parameters are the solar panel parameters at Standard Test Conditions (STC): Irradiance = 1000 W/m^2, Cell temperature = 25°C

2) Calculate the clear-sky normal beam, horizontal diffuse, and horizontal global irradiance components using the Simplified Solis model
3) Use the Reindl model to calculate the incident irradiance on each solar panel
4) Scale the single-diode reference parameters for each panel given the calculated incident irradiance
5) Solve Equation 8 with Lambert W function and use golden-selection search to find the maximum power point for each panel

The received power was simulated for the 2016 summer and winter solstices, as well as the spring and fall equinoxes. Figure 6 compares the power received for the solstices over a daylong period. The results demonstrate the variation in available solar energy due to the time of year as well as the differences in direct and diffuse irradiance components. The lower the sun's elevation angle is for a particular day (smaller solar zenith angle θ_z), the larger the ratio of direct to diffuse irradiance will be. This means in winter months quad-rotor state will bring in a similar amount of energy compared to fixed-wing. Additionally, Table IV includes the total energy harvested over each day for all 2016 equinoxes and solstices. Table IV also lists the ratio of energy available in fixed-wing and quad-rotor states. The results show that even though all panels in quad-rotor state have high surface tilt angles (less view of the sky), an appreciable amount of power is available due to the diffuse radiation.

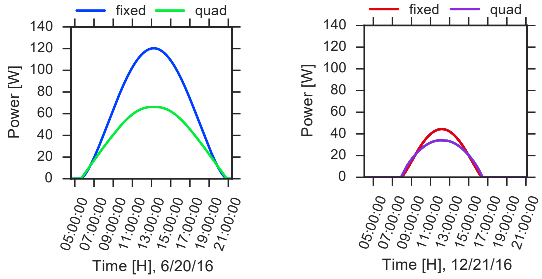

(a) Summer solstice **(b)** Winter solstice

Fig. 6: Simulation of day-long available solar power in fixed-wing and quad-rotor states for 2016 summer (a_{700}=0.147 w=3.5) and winter (a_{700}=0.061, w=0.8) solstices.

State	3/19/16	6/20/16	9/22/16	12/21/16
Fixed-wing [Wh]	672.17	1034.34	643.38	229.63
Quad-rotor [Wh]	459.91	628.01	436.04	200.54
Ratio	1.462	1.647	1.476	1.145

TABLE IV: Harvested energy in fixed-wing and quad-rotor states for 2016 spring (a_{700}=0.09, w=1) and fall (a_{700}=0.105, w=1.6) equinoxes, and summer and winter solstices. Location: St. Paul, MN.

IV. PROPULSION

The SUAV-Q propulsion system has been designed to provide efficient mobility across all flight modes by leveraging the efficiency gains that come from optimally controlling the propeller blades' collective pitch angle as shown in Figure 7(b). To validate the previous propulsion design work in [5] and [6], preliminary fixed-wing flight tests were conducted with propellers of various stationary pitch angles to verify efficiency gain as a function of blade pitch. In each test, the SUAV-Q was hand-launched, flown in a straight line to most accurately capture level flight behavior, and then landed. A performance comparison of two propeller pitch angles in Figure 7 shows that the 20°-pitch propeller has a notably lower average level-flight power than the stock-pitch propeller during the time that the airspeed is approximately constant. Nevertheless, further testing is needed to confirm better estimates for the power-optimum level flight power.

(a) SUAV-Q fixed-wing level flight

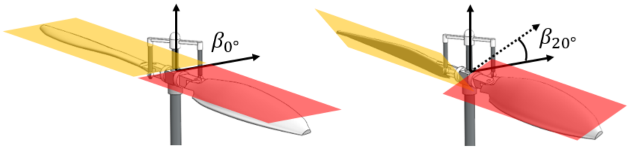

(b) VPP system in stock 0° and 20° β angles

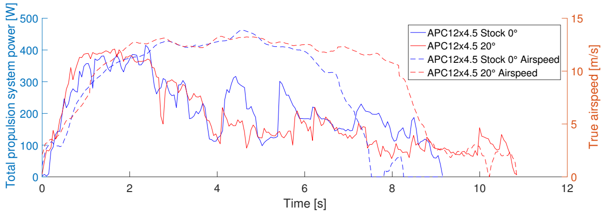

(c) Total propulsion system power consumption at $\beta = 0^\circ$ and $\beta = 20^\circ$

Fig. 7: Power consumption of two different propulsion systems at $\beta = 0^\circ$ and $\beta = 20^\circ$ for a fixed-wing hand-launched takeoff. Level flight power is estimated at 213.82W at $\beta = 0^\circ$ and 131.92W at $\beta = 20^\circ$.

In addition to the efficiency evaluation, an investigation was conducted on the actuation limits of the propulsion system due to energy constraints. Knowing the aircraft's actuation limits on a moment-by-moment basis allows the SUAV-Q to be used to its maximum potential. Each motor-propeller pair on the SUAV-Q is controlled by a throttle signal to the ESC and a signal regulating the pitch angle of the propeller. If the throttle command is fixed at its maximum value, specification of a range of pitch angles and air speeds will specify the performance ceiling at the corresponding battery state of charge (SOC).

To relate battery SOC and propulsion performance limits, analytical models were chosen for the system subcomponents and were linked together to simulate steady-state propulsion characteristics at maximum throttle command. The battery model developed in [16] was used to take into account factors such as voltage sag and battery capacity depletion during discharge. The model in this paper was simplified such that the open-circuit voltage is approximately linear with SOC. The ESC efficiency model was developed from data presented in [17]. The motor and propeller analysis tool, QPROP [18], was incorporated for steady-state modeling of the propulsive load characteristics.

The performance ceiling was calculated by sweeping across pitch angles ($\beta = -10^\circ$ to 25°) and air speeds ($v = 0$ to 15 m/s) at maximum throttle. The resulting point cloud in $\mathbb{R}^3$ was fit to a polynomial surface as in Figure 8 with linear

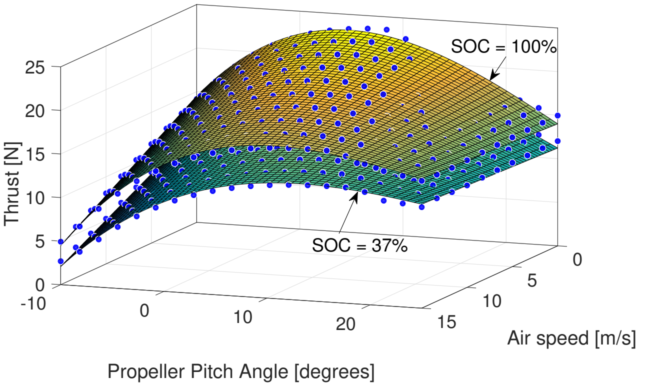

Fig. 8: Simulation of thrust limits at different charge states. The blue points indicate simulated states from the propulsion system numerical model, while the colored mesh denotes the regressed polynomial fit to the data. Note that while the z-axis denotes thrust specifically, the coordinates given by the four variables present in the plot are sufficient to define the entire propulsion system state uniquely.

dependence on v and cubic on β. This process was repeated every 5% change in SOC. The lowest R-squared value for the fit was 0.97, and these fits were linearly correlated with SOC via Equation 10 with parameters[4] **m** and **b**.

$$\hat{T}_{max} = \left[1, v, \beta, v\beta, \beta^2, v\beta^2, \beta^3\right] \left[\begin{bmatrix} m_1 \\ \vdots \\ m_7 \end{bmatrix} SOC + \begin{bmatrix} b_1 \\ \vdots \\ b_7 \end{bmatrix} \right] \tag{10}$$

Although Equation 10 relates v and β specifically to maximum estimated thrust $\hat{T}_{max}$, note that v, β, $\hat{T}_{max}$, and SOC are sufficient to define a unique propulsion state, and can thus be used to estimate any propulsion state quantity.

While Equation 10 describes the limits of one motor-propeller pair, the model can be generalized to describe the limits of a set of propulsion systems that are connected to a central battery. To do this, the SOC value in equation 10 is replaced with an effective SOC that is adjusted according to the total current drawn from the motor.

V. MAXIMUM POWER POINT TRACKING

The power extracted from solar panels is load-dependent and an electronics module called a maximum power point tracker (MPPT) is used to adjust the load seen by the solar panels. The optimum load (or maximum power point) is constantly changing due to flight dynamics and environmental conditions. An MPPT is typically a switch-mode converter running a maximum power tracking algorithm. The total MPPT efficiency depends on both the hardware efficiency η_h and the tracking algorithm efficiency η_a, where the total efficiency is given by the product $\eta_h \eta_a$. Initial efficiency results of a custom MPPT designed for 30-watt power levels were presented in [5]. In this section, simulated and experimental results characterizing the custom MPPT efficiency over the entire operating range of the battery are presented. Additionally, the steady-state and dynamic algorithm efficiency for three common tracking algorithms are evaluated.

A. Hardware Efficiency

A major challenge in designing the MPPT hardware is achieving both low mass and high efficiency. Because the solar panel on each wing segment will always output a lower voltage than the 4s2p battery pack, the MPPT design uses a boost converter topology. The relationship between the input and output voltage for a boost converter is given by,

$$\frac{V_{out}}{V_{in}} = \frac{1}{1-d} \tag{11}$$

where d is the duty cycle of the pulse-width-modulated (PWM) control signal.

A schematic for a boost converter, shown in Figure 9, contains an inductor L, diode D, power MOSFET M, input capacitor C_{in}, and output capacitor C_{out}. The inductor typically makes up a large portion of the MPPT mass and should be kept small to minimize its effect on flight power consumption. However, small inductor size results in increased current ripple and series resistance, which lowers converter efficiency. In addition, it is desired that the MPPT efficiency be high across all operating conditions. Figure 10a is a simulation of the MPPT efficiency operation across all operational irradiances and battery voltages. The simulation used equations for conduction and switching losses defined in [19] and component values shown in Table V.

C_{in}	66 μF
L	22 μH
M	IPT004N03L
D	PMEG045V100EPD
C_{out}	284 μF

TABLE V: Custom MPPT component values

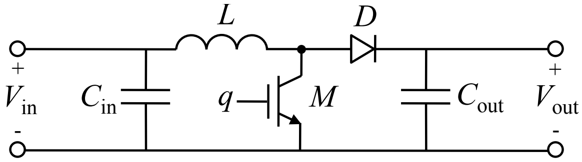

Fig. 9: Schematic of a basic boost converter. Signal q is the gate drive signal, determining the switching frequency ($\frac{1}{T_s}$) and duty ratio (d) of the converter.

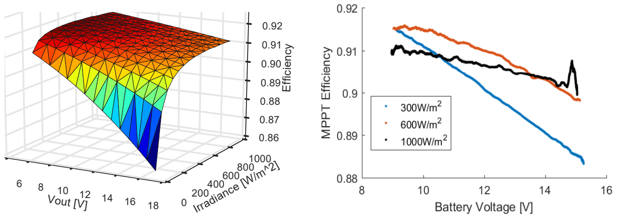

(a) MPPT Efficiency Simulation **(b)** MPPT Efficiency Test

Fig. 10: a) Simulation of MPPT efficiency considering inductor series resistance R_{Ls}, MOSFET drain-source resistance $R_{DS,on}$, diode forward losses, and switching losses. b) An MPPT was set to operate at the maximum power points corresponding to 1000W/m^2, 600W/m^2, and 300W/m^2. The efficiency over the range of battery voltages was measured. The experimental data follows closely with the simulated performance in (a).

The simulation results show that efficiency remains constant over a majority of the output voltage range. Only at very low irradiance and high output voltages does the efficiency

---

[4] Values for parameters $[m_1 \ldots m_7], [b_1 \ldots b_7]$ are, respectively, $[1.02e1, -1.10e{-1}, 7.34e{-2}, 7.70e{-3}, -1.93e{-3}, -9.96e{-5}, 3.69e{-4}]$, $[1.21e1, -4.19e{-1}, 2.66e{-1}, 1.22e{-2}, -2.07e{-2}, 2.29e{-4}, 1.60e{-4}]$.

drop below 90% due to large current through the inductor winding at high boost ratios V_{out}/V_{in}.

To characterize the efficiency of the custom MPPT, three experimental tests imitating the simulation were performed with the same component values listed in Table V. In each test, the MPPT was used to supply power to a 4s1p Li-ion pack and resistive load. The load was selected to slowly discharge the fully-charged battery, causing the output voltage to sweep from the maximum operating voltage of 15V to a minimum of 9V. The input voltage and current corresponded to a maximum power point of the SunPower E60 single-diode model of Section III for irradiances of 300 W/m^2, 600 W/m^2, and 1000 W/m^2 at a panel temperature of 25 °C. The results are plotted in Figure 10b and show that the efficiency of the MPPT is roughly constant with an average of 90.14% over the operational range and followed the simulated efficiency very closely. For the chosen components, this provides a η_h = 0.9014 which can be applied to the values in Table IV to find the available energy when using this MPPT.

B. Tracking Algorithm Efficiency

The maximum power point (MPP) of a solar array varies greatly with irradiance and temperature, requiring the MPPT to continually adjust the load seen by the array. To do this, the MPPT runs an MPP tracking algorithm. There are many proposed MPP tracking techniques as reviewed by [20][21], however, many are difficult to implement on the SUAV-Q platform due to complexity or the requirement of additional sensed parameters such as cell temperature [22]. For these reasons fixed-step perturb and observe (FSPO), adaptive-step perturb and observe (ASPO), and incremental conductance (IC) were chosen as they are easy to implement, require no additional measurements, and can easily incorporate system-level information through sensitivity gains in the algorithms.

In [5] FSPO and ASPO were simulated and the results indicated that ASPO is superior for the SUAV-Q platform due to its good dynamic irradiance performance. However, IC has also been shown to work well in dynamic irradiance conditions [21]. Consequently, all three were implemented on the same test system and an algorithm efficiency was estimated. The test system consisted of two solar arrays fixed along the same plane. An MPPT was attached to one array while the other array was short-circuited. The platform was then tested outdoors in direct sunlight and the voltage and currents for both arrays were recorded. Using the equations described in III-B, the short circuit current was used to estimate the maximum power the arrays could generate. This estimated maximum power was then compared with the power generated by the solar array running the tracking algorithm. The resulting FSPO, ASPO, and IC algorithm efficiencies were found to be 0.9291, 0.9277, and 0.9069, respectively. Using FSPO gives the MPPT an overall efficiency of 0.8375.

VI. PULSE CHARGING

In addition to energy collection efficiency, efficient energy storage is also vital. The most common form of Lithium Ion (Li-ion) battery charging is constant current-constant voltage (CC-CV), due to simplicity and ease of implementation [23]. However, CC-CV can lead to accelerated capacity loss, and increased cell impedance. Pulse charging is a charging technique that mitigates many of these issues and increases battery life by reducing the amount of total battery capacity lost during each charge cycle [24]. This section presents the hardware design of a pulse charging circuit and compares pulse charging to CC-CV with empirical data.

A. Hardware

The hardware implementation of the pulse charger circuit consisted of a MOSFET (CSD18504Q5A), current sense amplifier (MAX9611), and a microcontroller (ATMEGA328P).

The pulse charge algorithm used for testing and proof of concept was a fixed-frequency, fixed-duty-cycle pulse. In future implementations, the measured voltage and current would be used in real time to determine battery SOC, and an adaptive algorithm would control the pulse pattern [25][26]. In this adaptive method, equations which govern the response of the battery to a current step (such as Sand's equation and Cottrell's equation [27]) would be used for determining the optimum pulse frequency. In order to make full use of these optimizations, a more complex 4-phase pulse (as shown in Figure 11) would be implemented using a parallel MOSFET to provide a constant current discharge pulse (shown in Figure 12).

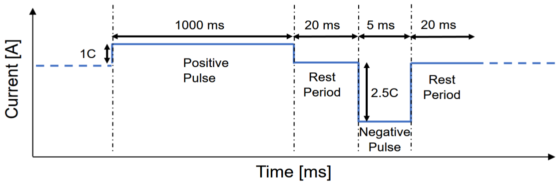

Fig. 11: Four-stage pulse charging design.

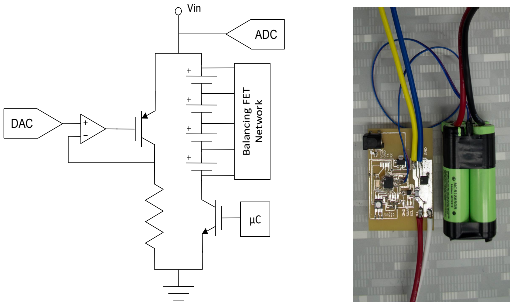

Fig. 12: Future implementation of pulse charging circuit (left) and proof of concept circuit used for gathering experimental data (right).

B. Experiments

The pulse charging method was tested and compared against a standard CC-CV charging method as shown in Figure 13. Pulse charging exhibited highly desirable characteristics over CC-CV techniques by matching charge times while also extending battery charge cycle life and higher current delivery.

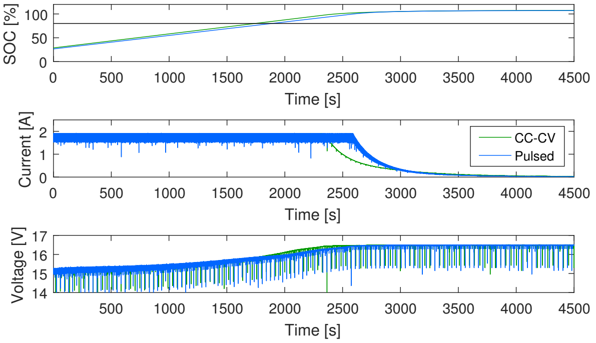

Fig. 13: Voltage, current, and SOC of a 4S ($V_N = 14.8V$), 1.8 Ah Lithium Polymer (Li-Po) battery pack, charged at 1C using CC-CV (green line) and charged at 1C maximum current. The pulsed current has a period of 1 s and a 40 ms off time (blue line). This figure shows that both CC-CV and pulsed charging methods are able to deliver a complete charge in an equivelent amount of time.

VII. CONCLUSION

This paper presents a thorough energy characterization of the subsystems on the SUAV-Q platform. The presented models for solar irradiance and solar cells allow for accurate prediction of collected solar energy for complex aircraft configurations at different times of day and year. Test flights indicated a significant increase in level-flight efficiency due to variable-pitch propulsion. The propulsion model quantified the propulsive ceiling due to available energy limits. Simulations and experiments indicated that the MPPT hardware retains efficiencies over 90% across the majority of irradiance and boost conditions. Experimental investigation of candidate MPPT algorithms demonstrated that fixed-step was the most efficient algorithm in steady-state of the three. Testbed experiments indicated that pulse charging provides increased cycle life without compromising charge time.

Future investigation of power characteristics will involve further work on all subsystems; extensive flight tests will be used to verify the proposed models of irradiance, solar cells, and propulsion limits, along with onboard testing of variable-pitch propulsion, MPPT hardware and tracking algorithms, and pulse charging hardware. Control algorithms utilizing these models and hardware will be used to optimize system efficiency across all flight states.

VIII. ACKNOWLEDGEMENTS

This material is based upon work supported by the National Science Foundation through grants #IIP-0934327, #IIS-1017344, #IIP-1332133, #IIS-1427014, #IIP-1432957, #OISE-1551059, #CNS-1514626, #CNS-1531330, and #CNS-1544887. Ruben D'Sa was supported by a National Science Foundation Graduate Research Fellowship No. 00039202.

REFERENCES

[1] P. Oettershagen, A. Melzer, T. Mantel, K. Rudin, T. Stastny, B. Wawrzacz, T. Hinzmann, K. Alexis, and R. Siegwart, "Perpetual Flight with a Small Solar-Powered UAV: Flight Results, Performance Analysis and Model Validation." IEEE Aerospace Conference, 2016, 2016.

[2] W. Fredericks, M. Moore, and R. Busan, "Benefits of Hybrid-Electric Propulsion to Achieve 4x Cruise Efficiency for a VTOL UAV," in *International Power Lift Conference, AIAA Aviation*, 2013, pp. 171–191.

[3] A. Oosedo, S. Abiko, A. Konno, T. Koizumi, T. Furui, and M. Uchiyama, "Development of a Quad Rotor Tail-Sitter VTOL UAV without Control Surfaces and Experimental Verification," in *IEEE International Conference on Robotics and Automation (ICRA)*, 2013, pp. 317–322.

[4] R. D'Sa, D. Jenson, and N. Papanikolopoulos, "SUAV:Q - A Hybrid Approach To Solar-Powered Flight," *IEEE International Conference on Robotics and Automation (ICRA)*, pp. 3288–3294, May 2016.

[5] R. D'Sa, D. Jenson, T. Henderson, J. Kilian, B. Schulz, M. Calvert, T. Heller, and N. Papanikolopoulos, "SUAV:Q - An Improved Design for a Transformable Solar-Powered UAV," *IEEE/RSJ International Conference on Intelligent Robots and Systems (IROS)*, October 2016.

[6] R. D'Sa, T. Henderson, D. Jenson, M. Calvert, T. Heller, B. Schulz, J. Kilian, and N. Papanikolopoulos, "Design and Experiments for a Transformable Solar-UAV," *IEEE International Conference on Robotics and Automation (ICRA)*, May 2017.

[7] J. A. Duffie and W. A. Beckman, *Solar Engineering of Thermal Processes*, 3rd ed. Wiley, 2006.

[8] P. Ineichen, "A Broadband Simplified Version of the Solis Clear Sky Model," *Solar Energy 82*, p. 758 762, 2008.

[9] S. Wilcox and W. Marion, "Users Manual for TMY3 Data Sets," 2005, nREL/TP-581-43156.

[10] W. F. Holmgren, R. W. Andrews, A. T. Lorenzo, and J. S. Stein, "PVLIB Python 2015," *42nd Photovoltaic Specialists Conference*, 2015.

[11] J. Nou, R. Chauvin, S. Thil, J. Eynard, and S. Grieu, "Clear-sky Irradiance Model for Real-Time Sky Imager Application," *Energy Procedia*, vol. 69, pp. 1999–2008, 2015.

[12] W. De Soto, S. Klein, and W. Beckman, "Improvement and Validation of a Model for Photovoltaic Array Performance," *Solar Energy 80*, 2006.

[13] U. Eicker, *Solar Technologies for Buildings*, 1st ed. Wiley, 2003.

[14] N. Femia, G. Petrone, G. Spagnuolo, and M. Vitelli, *Power Electronics and Control Techniques for Maximum Energy Harvesting in Photovoltaic Systems*. CRC Press, 2012.

[15] A. Jain and A. Kapoor, "Exact Analytical Solutions of the Parameters of Real Solar Cells using Lambert W-Function," *Solar Energy Materials and Solar Cells 81*, pp. 269–277, 2004.

[16] M. Chen and G. A. Rincon-Mora, "Accurate Electrical Battery Model Capable of Predicting Runtime and I-V Performance," *IEEE Transactions on Energy Conversion*, vol. 21, no. 2, pp. 504–511, June 2006.

[17] C. R. Green and R. A. McDonald, "Modeling and Test of the Efficiency of Electronic Speed Controllers for Brushless DC Motors," in *15th AIAA Aviation Technology, Integration, and Operations Conference*, 2015, p. 3191.

[18] M. Drela, "QPROP Formulation," http://web.mit.edu/drela/Public/web/qprop/qprop_theory.pdf, 2006.

[19] T. Eichhorn, "Boost Converter Efficiency Through Accurate Calculations," in *Power Electronics Technology*, 2008, pp. 30–35.

[20] S. Agarwal and M. Jamil, "A Comparison of Photovoltaic Maximum Power Point Techniques," in *2015 Annual IEEE India Conference (INDICON)*, Dec 2015, pp. 439–449.

[21] A. R. Reisi, M. H. Moradi, and S. Jamasb, "Classification and Comparison of Maximum Power Point Tracking Techniques for Photovoltaic System: A Review," *Renewable and Sustainable Energy Reviews*, vol. 19, pp. 433–443, 2013.

[22] M. H. Moradi and A. R. Reisi, "A Hybrid Maximum Power Point Tracking Method for Photovoltaic Systems," *Solar Energy*, vol. 85, no. 11, pp. 2965–2976, 2011.

[23] D. Linden and T. B. Reddy, *Handbook of Batteries*, 3rd ed. McGrawHill, 2002.

[24] B. N. Popov, P. Ramadass, B. Haran, and R. E. While, "Capacity Fade Studies of Lithium Ion Cells," 2002. [Online]. Available: http://www.che.sc.edu/faculty/popov/drbnp/Ramadass/June2002.pdf

[25] F. Naznin, "State of Charge (SOC) Governed Fast Charging Method for Lithium Based Batteries," in *COMSOL*, 2013.

[26] B. K. Purushothaman and U. Landauz, "Rapid Charging of Lithium-Ion Batteries Using Pulsed Currents a theoretical analysis," *Journal of The Electrochemical Society*, pp. 533–542, 2006.

[27] T. Sritharan, "Impact of Current Waveforms on Battery Behaviour," Masters Thesis, Department of Electrical and Computer Engineering, University of Toronto, 2012.